

# Tomographic reconstruction of a disease transmission landscape via GPS recorded random paths

Jairo Diaz-Rodriguez<sup>1</sup>, Juan Pablo Gomez<sup>2</sup>, Jeremy P. Orange<sup>3,4</sup>,  
Nathan D. Burkett-Cadena<sup>5</sup>, Samantha M. Wisely<sup>6</sup>, Jason  
K. Blackburn<sup>3,4</sup> and Sylvain Sardy<sup>7</sup>

<sup>1</sup>*Department of Mathematics and Statistics, York University, Canada, e-mail: [jdiazrod@yorku.ca](mailto:jdiazrod@yorku.ca)*

<sup>2</sup>*Departamento de Química y Biología, Universidad del Norte, Colombia, e-mail: [echeverrip@uninorte.edu.co](mailto:echeverrip@uninorte.edu.co)*

<sup>3</sup>*Spatial Epidemiology & Ecology Research Laboratory, Department of Geography, University of Florida, USA, e-mail: [jporange2@ufl.edu](mailto:jporange2@ufl.edu)*

<sup>4</sup>*Emerging Pathogens Institute, University of Florida, USA, e-mail: [jkblackburn@ufl.edu](mailto:jkblackburn@ufl.edu)*

<sup>5</sup>*Florida Medical Entomology Laboratory, University of Florida, USA, e-mail: [nburkettcadena@ufl.edu](mailto:nburkettcadena@ufl.edu)*

<sup>6</sup>*Department of Wildlife Ecology and Conservation, University of Florida, USA, e-mail: [wisely@ufl.edu](mailto:wisely@ufl.edu)*

<sup>7</sup>*Mathematics Section, Université de Genève, Switzerland, e-mail: [sylvain.sardy@unige.ch](mailto:sylvain.sardy@unige.ch)*

**Abstract:** Identifying areas in a landscape where individuals have a higher likelihood of disease infection is key to managing diseases. Unlike conventional methods relying on ecological assumptions, we perform a novel epidemiological tomography for the estimation of landscape propensity to disease infection, using GPS animal tracks in a manner analogous to tomographic techniques in positron emission tomography (PET). Treating tracking data as random Radon transforms, we analyze Cervid movements in a game preserve, paired with antibody levels for epizootic hemorrhagic disease virus (EHDV)—a vector-borne disease transmitted by biting midges. After discretizing the field and building the regression matrix of the time spent by each deer (row) at each point of the lattice (column), we model the binary response (infected or not) as a binomial linear inverse problem where spatial coherence is enforced with a total variation regularization. The smoothness of the reconstructed propensity map is selected by the quantile universal threshold. To address limitations of small sample sizes and evaluate significance of our estimates, we quantify uncertainty using a bootstrap-based data augmentation procedure. Our method outperforms alternative ones when using simulated and real data. This tomographic framework is novel, with no established statistical methods tailored for such data.

**Keywords and phrases:** disease transmission, GPS data, inverse problems, quantile universal threshold, total variation, tomography.

## 1. Introduction

### 1.1. Epidemiological background

Predicting spatial disease risk is crucial for managing human, livestock, and wildlife diseases (Morris & Blackburn 2016). Traditionally, spatial prediction of infectious diseases has been understudied (Ostfeld et al. 2005, Kirby et al. 2017), but advances in algorithms and technology have improved spatial inferences of disease dynamics (Ostfeld et al. 2005, Riley et al. 2015, Kirby et al. 2017). Many studies focus on directly transmitted diseases, yet numerous significant epidemics and zoonoses are indirectly transmitted, relying on vectors or environmental reservoirs (Hollingsworth et al. 2015). Examples include vector-borne diseases like malaria and Lyme disease (Torres-Sorando & Rodriguez 1997, Killilea et al. 2008, Messina et al. 2015), and non-vector-borne diseases like anthrax and cholera (Ostfeld et al. 2005).

Inferences about the risk of indirectly transmitted diseases often depend on the spatial distribution of cases or prior knowledge about their ecology and dynamics. Spatially explicit compartmental models require prior knowledge of transmission rates or hypotheses about disease spread, which may not be available for emerging diseases (Harvell et al. 2002, Patz et al. 2008). Understanding how animals use the landscape is essential for managing these diseases (Dinh et al. 2020, Orange, Dinh, Peters, Wisely & Blackburn 2021), as it helps describe the distribution and spatial autocorrelation of animal locations over time (de Thoisy et al. 2020, Albery et al. 2022, Dougherty et al. 2018).

Common methods like Maxent and GARP link climatic conditions to the physiological constraints of pathogens and vectors to predict disease presence (Ahmed et al. 2015, Elith et al. 2011, Stockwell 1999). However, predicting disease risk based solely on presence data is limited, as these points are typically identified infected individuals (Ostfeld et al. 2005). Incorporating animal home range and habitat selection has proven useful in identifying transmission risk of wildlife zoonoses (Ragg & Moller 2000, Dougherty et al. 2022). Coupling individual disease status with animal movements can better identify high-risk areas (Ostfeld et al. 2005), yet host movements are seldom included in disease niche modeling or spatial risk prediction.

Recent approaches have begun using movement data from infected individuals to infer areas of higher infection risk (Dougherty et al. 2018, Brdar et al. 2016, Frias-Martinez et al. 2012). While some methods include spatially explicit compartmental models (Lima et al. 2015), they often rely on underlying assumptions about disease dynamics. In this study, we propose a novel method to map disease risk using animal movement and health status without relying on prior ecological assumptions. We demonstrate this method with simulations and data from native and exotic cervid species infected with Epizootic Hemorrhagic Disease Virus (EHDV) on a Florida hunting ranch.

### 1.2. Cervid movement and EHDV prevalence data collection

In a 172-ha high-fenced ranch in Florida, USA dedicated to big-game hunting, move freely white-tailed (WTD), Pere David (ED), Fallow (DD) and Elk deer (CC). A high prevalence of several serotypes of EHDV causes severe clinical signs such as hemorrhaging, edema, hoof-sloughing, oral lesions and death, principally in WTD, but it affects other cervid species as well. EHDV is transmitted by biting midges from the genus *Culicoides* and, in southeastern United States, *Culicoides stellifer* and *Culicoides venustus* have been identified as the competent EHDV vectors. There has been substantial research on this high-fenced ranch regarding host behavior, spatial movement and vector behavior and ecology (McGregor, Stenn, Saylor, Blosser, Blackburn, Wisely & Burkett-Cadena 2019, Dinh, Gomez, Orange, Morris, Saylor, McGregor, Blosser, Burkett-Cadena, Wisely & Blackburn 2021, McGregor, Sloyer, Saylor, Goodfriend, Krauer Campos, Acevedo, Zhang, Mathias, Wisely & Burkett-Cadena 2019, Orange, Dinh, Peters, Wisely & Blackburn 2021, Dinh et al. 2020, Dinh, Orange, Peters, Wisely & Blackburn 2021). The prevalence of EHDV in WTD and other exotic species has also been described (Cauvin et al. 2020, Orange, Dinh, Goodfriend, Citino, Wisely & Blackburn 2021), but to date, disease risk on the ranch has been estimated by inferring resource selection in deer and overlap with areas of high biting midge abundance.

To investigate disease transmission, we used data from 26 GPS collared WTD (8 females, 18 males) tracked for an average of 149 days during 2015 and 2016. Individuals were captured and GPS collared in the spring, ahead of the EHDV transmission season (Dinh et al. 2020) and recaptured in fall to remove the collars. GPS collars were programmed to collect a GPS location every 15 or 120 minutes (Cauvin et al. 2020, Dinh et al. 2020). Animals were immobilized with cartridge or air powered darts, monitored, collared, bled, and released (see Cauvin et al. 2020, Dinh et al. 2020 for details about capture procedures). A blood sample was obtained from individual at the time of initial capture and again when GPS collars were recovered. Each blood sample was tested for the presence of EHDV-1, EHDV-2 and EHDV-6 antibody titers using a virus neutralization test performed at Texas A&M University (Stallknecht et al. 1996; see Cauvin et al. 2020 for details). We classified animals as positive or negative for each virus type using previous cutoffs (Cauvin et al. 2020). Four individuals were tracked during both years allowing us to use the tracks as independent replicates to increase our sample size to 30 animals (Appendix C). We pre-processed the raw GPS tracks and excluded those of seropositive individuals at both collection times. All tracks were interpolated to 15 minutes. At the end the data consisted of 27 tracks for EHDV-1 infected animals, 22 for EHDV-2, and 30 for EHDV-6. The deer capture and handling protocols were developed by JKB and the ranch wildlife manager and approved by the Institutional Animal Care and Use Committee at the University of Florida (UF IACUC Protocols #201508838 and #201609412).

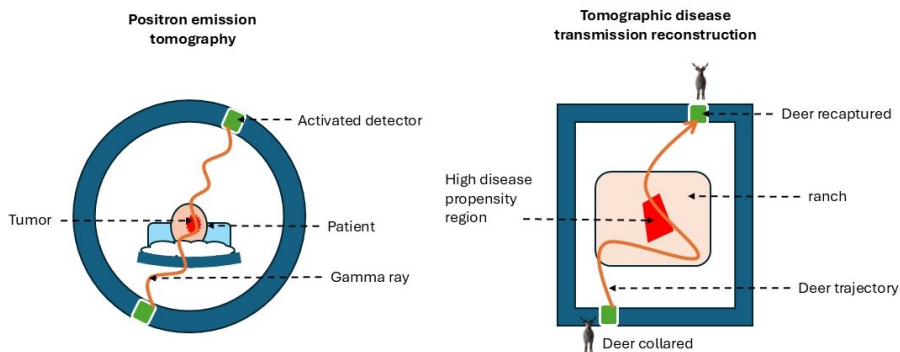


FIG 1. An analogy between Positron Emission Tomography (left) and the tomographic reconstruction of a disease propensity map (right): Deer moving in a ranch represent gamma rays traveling through a patient. Whether a deer gets infected is like the signals detected in PET. The goal is to reconstruct the high-propensity area, similar to identifying a tumor.

### 1.3. Data transformation

If, for a second, we imagine that these deer could be trained to enter the ranch at designed locations, walk along lines  $L_i$  and exits the ranch at the end of their straight walks, then the information whether the deer contracted the disease along these lines could help map the disease propensity on the ranch and each deer walking along a line would essentially have calculated the Radon transform  $R_\mu(L_i) = \int_{L_i} \mu(u, v) \sqrt{du^2 + dv^2}$  of the propensity map  $\mu(u, v)$  as a function of locations  $(u, v)$ , along the  $L_i$ , for deer and line  $i = 1, \dots, n$ . This is what positron emission tomography (PET) is doing with rays instead of deer, for non-invasive brain imaging for instance (Figure 1).

While this is not feasible with deer because they do not move along straight lines, pet-imaging would be possible with well trained domesticated animals, but at the price of training them to walk along predetermined straight lines. Deer cannot be trained, but, while moving freely along random paths  $P_i$ , deer gather information about  $\mu(u, v)$  with the Radon transform  $R_\mu(P_i) = \int_{P_i} \mu(u, v) \sqrt{du^2 + dv^2}$ , for deer and path  $i = 1, \dots, n$ . If one can extract information from GPS locations of individuals moving freely in a medium along random paths and contracting a disease or not, then one performs some imaging of the medium, here the disease propensity map.

Going back to the deer movement data, each deer has a blood test at time 0 leading to concentrations of four different antibodies  $c_{i,m}(0)$ , and at time  $t_i$  leading to concentrations  $c_{i,m}(t_i)$ ,  $m = 1, \dots, 3$  (EHDV-1, EHDV-2 and EHDV-6 antibodies). From these concentrations, the binary responses  $y_{i,m} = 1_{\{c_{i,m}(t_i) > c_{i,m}(0)\}}$  declares whether or not the  $i$ th individual got infected by virus  $m$  during the time period, for  $i = 1, \dots, n$  and  $m = 1, \dots, 3$ . Individuals move differently in the fenced area  $\Omega$ , as observed by the GPS tracking system. To map the spatial variability in infection propensity  $\mu$ , the fenced area  $\Omega$  is spatially

discretized and partitioned over equal small units  $\omega^{j,k}$  indexed by latitude  $j$  and longitude  $k$ , for  $(j, k) \in \mathcal{F}$ . The level of discretization  $p = |\mathcal{F}|$  is chosen by the practitioner: the larger  $p$ , the finer the spatial discretization, but the more parameters to estimate. Correspondingly, each area  $\omega^{j,k}$  has the propensity  $\mu(\omega^{j,k})$  of contaminating a species with a disease during a unit time period, where  $\mu$  is a function of localization  $\omega^{j,k}$  in  $\Omega$ . Using the GPS recordings, one can, for each individual  $i$ , aggregate the total time  $x_i^{j,k}$  spent in each small area  $\omega^{j,k}$  between its starting time until time  $t_i$ ; so let  $\mathbf{x}_i = \{x_i^{j,k}\}_{(j,k) \in \mathcal{F}}$  be the vector of total time spent in location  $\omega^{j,k}$  for individual  $i$ , for  $i = 1, \dots, n$ . The goal is to estimate the propensity maps  $\boldsymbol{\mu}_m = \{\mu_m(\omega^{j,k})\}_{(j,k) \in \mathcal{F}}$  ( $m = 1, \dots, 3$ , one map per EHDV virus) based on the information contained in the data  $(y_i, \mathbf{x}_i)_{i=1, \dots, n}$ . We performed this data transformation process (we provide the resultant  $X$  and  $y$  for each dataset in the supplementary materials) to the EHDV-1, EHDV-2 and EHDV-6 datasets.

#### 1.4. Our approach

Individuals randomly moving in the field are analogous to tomographic rays traveling across a medium, and the resulting binary output indicating whether or not the animals became infected are akin to sensor readings (Figure 1). So we aim at retrieving the disease propensity map, in the spirit of inverse problems such as positron emission tomography (PET). To the best of our knowledge, our approach is novel to disease mapping and indirect risk estimation for the data we described.

Following on the data preprocessing proposed in Section 1.3, we present our approach in the following way. In Section 2, we model the data with a generalized linear model regularized by a total variation penalty to enforce spatial coherence in the propensity map, we discuss the selection of the regularization parameter and propose an algorithm to solve the convex optimization problem, we derive a statistical test for a constant propensity map, and we show how to perform uncertainty quantification. In Section 3, we perform a Monte Carlo simulation to empirically compare three methods of estimation with three different asymptotics: increasing sample size, increasing spatial resolution, and increasing frequency recording. In Section 4, we analyze the deer data of Section 1.2. In Section 5, we summarize our contributions and point to generalizations of our approach. The research is reproducible (see Supplementary Material).

## 2. Total variation regularization of GLM

### 2.1. Model

Since the three EHDV serotype antibodies considered have their own specificities, three separate models are estimated, so we call the disease marker  $y_i \in \{0, 1\}$  (instead of  $y_{i,1}$  for EHDV-1,  $y_{i,2}$  for EHDV-2 and  $y_{i,3}$  for EHDV-6)

for  $i = 1, \dots, n$ . The classical approach for binary outcomes sees  $y_i$  as a realization of the random variable  $Y_i \sim \text{Bernoulli}(\epsilon_i)$ , where the probability  $\epsilon_i$  of being infected depends on where the  $i$ th individual spent its time in the fenced area. In particular  $\epsilon_i$  should be high if the  $i$ th individual spent long periods of time in areas of high infection propensity; in other words,  $\epsilon_i$  should be high when high total times  $x_i^{j,k}$  are observed in regions  $\omega^{j,k}$  where the unknown propensity  $\mu(\omega^{j,k})$  is high. A simple yet realistic model is the generalized linear model (Nelder & Wedderburn 1972) which assumes  $g(\epsilon_i) = \mathbf{x}_i^T \boldsymbol{\mu}$ , where the *logit* link  $g(\epsilon) = \log(\epsilon/(1-\epsilon))$  maps  $(0, 1)$  into  $\mathbb{R}$ . Letting  $\mathbf{Y} = (Y_1, \dots, Y_n)$  and  $X$  be the  $n \times p$  matrix which  $i$ th row is  $\mathbf{x}_i^T$ , the model is

$$\mathbf{Y} \sim \text{Bernoulli}(g^{-1}(X\boldsymbol{\mu})), \quad (1)$$

where  $\boldsymbol{\mu}$  is the unknown propensity vector. So the model can be seen as a tomographic linear inverse problem, for which the individuals are probing the space with their distinct movements reflected in the data matrix  $X$  of total times visiting the lattice system in  $\Omega$ . Instead of directly measuring the sources of where the virus is spreading, the information is indirectly measured on individuals living in potentially infecting areas.

## 2.2. Estimation

The vector of infection propensity  $\boldsymbol{\mu}$  has length  $p = |\mathcal{F}|$ , the cardinality of the lattice system that segments the fenced area  $\Omega$ . In our application the number of individuals is small, so we choose a fairly coarse segmentation of the fenced area into  $p = 200$  cells. Regularization is needed, and owing to the spatial structure of the problem, we impose a smoothness constraint on  $\boldsymbol{\mu}$ . Possible approaches models  $\mu$  as a linear combination of splines (Wahba 1990) or wavelets (Donoho 1995); kernel smoothing is another approach. We instead use total variation (TV) regularization (Rudin et al. 1992) for several reasons: first the domain is not rectangular, second epidemiologists prefer to identify constant propensity regions and third the propensity map may have some peaks (e.g., feeders) and discontinuities (e.g., along a river or a lake). TV provides a solution to these challenges as it easily adapts to a non-regular lattice, it performs segmentation (as it fits a piecewise constant function  $\mu$ ) and it allows sudden peaks and jumps.

To derive TV for our inverse problem, we define a system of neighborhood. An entry  $\mu_l$  of the vector of infection propensity  $\boldsymbol{\mu}$  corresponds to a small region  $\omega^{j,k}$  in  $\Omega$ . Each region  $(j, k)$  is associated to an entry of  $\boldsymbol{\mu}$ , call it  $l$ . Each region  $(j, k)$  (associated to  $l$ ) has neighbors: call  $\partial l$  the set of entries of  $\boldsymbol{\mu}$  corresponding to the neighbors of  $(j, k)$ . Because of the spatial structure of  $\boldsymbol{\mu}$  which maps the propensity of catching a virus somewhere in the ranch, one believes that the value of  $\mu_l$  is close to  $\mu_{l'}$  for  $l' \in \partial l$ ; here we consider the north-south-east-west neighborhood of a cell. TV imposes smoothness by solving

$$\min_{\boldsymbol{\mu} \in \mathbb{R}^p} -\log L(g^{-1}(X\boldsymbol{\mu}); \mathbf{y}) + \lambda \sum_{l=1}^p \sum_{l' \in \partial l} |\mu_l - \mu_{l'}|, \quad (2)$$

where  $L$  is the likelihood associated to (1),  $\mathbf{y}$  is the vector of infection indicator per individual,  $X$  is total time matrix per individual (lines) spent in area  $\omega^{j,k}$  (column), and  $\boldsymbol{\mu}$  is the two-dimensional surface to reconstruct. The regularization parameter  $\lambda > 0$  controls the smoothness of the estimate  $\hat{\boldsymbol{\mu}}_\lambda$  solution to (2). One standard selection of  $\lambda$  is cross-validation, which requires  $n$  large for a stable estimation. In our situation, the number  $n$  of individuals is rather small, so we employ the quantile universal threshold (Giacobino et al. 2017) that is geared towards estimating and testing the propensity map  $\boldsymbol{\mu}$ . The quantile universal threshold is based on calibrating a choice of  $\lambda$  under the null hypothesis  $H_0$  that the propensity map is constant (that is, no regions are more infectious than others): its goal is to retrieve a constant map with high probability under  $H_0$ . This choice of  $\lambda$  remains performant under alternative hypotheses as supported by the LASSO theory (Tibshirani 1996, Bühlmann & van de Geer 2011) and total variation (Rudin et al. 1992, Sardy & Monajemi 2019). Deriving the quantile universal threshold for our TV-estimator (2) is based on the following property.

*Property 2.1.* Assuming the entries of the responses  $\mathbf{y}$  are not all identical (all ones or all zeros), there exists a finite  $\lambda > 0$  for which the solution  $\hat{\boldsymbol{\mu}}_\lambda$  to (2) is a constant propensity map across  $\Omega$ . Moreover the smallest such  $\lambda$  is given by the zero-thresholding function

$$\lambda_0(\mathbf{y}, X) = \min_{\boldsymbol{\omega} \in \mathbb{R}^q} \|\boldsymbol{\omega}\|_\infty \quad (3)$$

$$\text{s.t. } X^T(\boldsymbol{\epsilon} - \mathbf{y}) + D^T\boldsymbol{\omega} = \mathbf{0}, \quad \boldsymbol{\epsilon} = g^{-1}(\hat{\beta}_0 X \mathbf{1}), \quad \hat{\beta}_0 = \underset{\beta_0 \in \mathbb{R}}{\operatorname{argmin}} h(\beta_0 \mathbf{1}; \mathbf{y}),$$

where  $h(\boldsymbol{\mu}; \mathbf{y}) = -\log L(g^{-1}(X\boldsymbol{\mu}); \mathbf{y})$  is the negative log-likelihood associated to model (1).

The quantile universal threshold for the estimator (2) can now be defined.

*Definition 2.2* (Quantile universal threshold). Given a matrix  $X$ , consider the random variable  $\Lambda = \lambda_0(\mathbf{Y}, X)$ , where  $\mathbf{Y}$  is given by model (1) under the assumption that  $\boldsymbol{\mu}$  is constant. For some small  $\alpha \in (0, 1)$ , the quantile universal threshold  $\lambda_\alpha^{\text{QUT}}$  is the upper  $\alpha$ -quantile of  $\Lambda$ .

Since  $\alpha$  corresponds to the false discovery rate (of detecting a non-constant map) under  $H_0$ , one chooses  $\alpha$  small, say  $\alpha = 0.05$ . The distribution of  $\Lambda$  is unknown however, so  $\lambda_\alpha^{\text{QUT}} = F_\Lambda^{-1}(1 - \alpha)$  has no closed form expression. Instead  $\lambda_\alpha^{\text{QUT}}$  can be estimated by Monte Carlo, simulating  $m$  realizations  $\mathbf{y}^{(1)}, \dots, \mathbf{y}^{(m)}$  of  $\mathbf{Y} \sim \text{Bernoulli}(g^{-1}(\beta_0 X \mathbf{1}))$  for some  $\beta_0$ , for instance  $\hat{\beta}_0 = \underset{\beta_0 \in \mathbb{R}}{\operatorname{argmin}} h(\beta_0 \mathbf{1}; \mathbf{y})$  for the data  $\mathbf{y}$  at hand. Then by calculating the corresponding  $\lambda_0(\mathbf{y}^{(1)}, X), \dots, \lambda_0(\mathbf{y}^{(m)}, X)$  and by taking their empirical upper  $\alpha$ -quantile, one estimates  $\lambda_\alpha^{\text{QUT}}$ . The zero-thresholding function implicitly defined in Property 2.1 requires solving the non-trivial optimization problem in (3);

fortunately, (3) can be rewritten as an easily solvable linear program, namely

$$\min_{\boldsymbol{\omega}, \lambda}(\mathbf{0}^T, 1) \begin{pmatrix} \boldsymbol{\omega} \\ \lambda \end{pmatrix} \quad \text{s.t.} \quad \begin{cases} \mathbf{u} \leq D^T \boldsymbol{\omega} \leq \mathbf{u} \\ \boldsymbol{\omega} - \lambda \mathbf{1} \leq \mathbf{0} \\ \boldsymbol{\omega} + \lambda \mathbf{1} \geq \mathbf{0} \\ \lambda \geq 0 \end{cases},$$

with  $\mathbf{u} = X^T(\mathbf{y} - \boldsymbol{\epsilon})$ ,  $\boldsymbol{\epsilon} = g^{-1}(\hat{\beta}_0 X \mathbf{1})$  and  $\hat{\beta}_0 = \operatorname{argmin}_{\beta_0 \in \mathbb{R}} h(\beta_0 \mathbf{1}; \mathbf{y})$ .

### 2.3. Testing

Testing is part of statistical inference, and the TV regularization of the GLM (2) allows to do so. A null hypothesis of interest is that there is no particular infectious region, in other words  $H_0 : \boldsymbol{\mu} = \mu_0 \mathbf{1}$  is constant. When  $n \geq p$ , the likelihood ratio test (either based on the asymptotic  $\chi^2$  distribution or on the exact distribution) comes to mind.

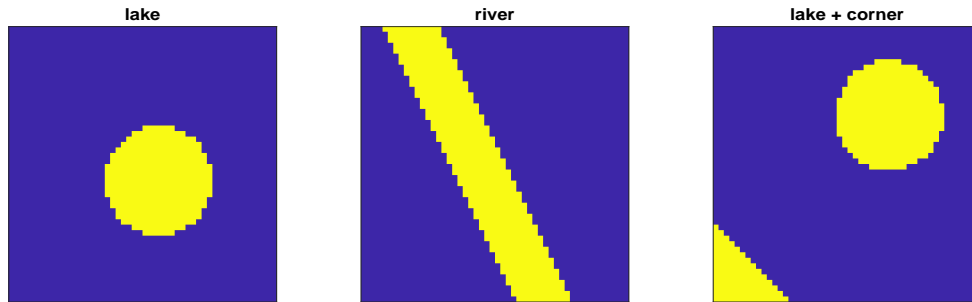
When the number of recorded deer is small and the field's mapping is finely discretized, we are in the  $p > n$  situation, however. To allow testing whether  $n > p$  or not, we propose the TV-test (Sardy et al. 2022) and based on total variation smoothing (Sardy & Monajemi 2019). The TV penalty term in (2) is zero for the constant infectious propensity. Hence, given  $\alpha \in (0, 1)$ , the test function

$$\phi(\mathbf{y}, X) = \begin{cases} 0 & \text{if } \lambda_0(\mathbf{y}, X) < \lambda_\alpha^{\text{QUT}} \\ 1 & \text{otherwise.} \end{cases} \quad (4)$$

tests  $H_0$  at level  $\alpha$ . One expects the TV-test to be more powerful than the likelihood ratio test for smooth (spatially homogeneous) alternative hypotheses (Sardy et al. 2022). A Monte Carlo simulation confirms it in Appendix B. As a side product, when the test is not rejected for some level  $\alpha$  means that the solution to (2) for  $\lambda = \lambda_\alpha^{\text{QUT}}$  is a constant propensity map without having to solve (2).

### 2.4. Data augmentation with uncertainty quantification

GPS sampling constraints often result in small sample sizes  $n$ . We address it by performing data augmentation, however, introducing additional variability. Furthermore, the estimation of the propensity  $\hat{\boldsymbol{\mu}}$  alone provides limited practical value for ecologists and practitioners. The estimate is conditional on the observed individuals and their random movements across the study area, which also introduces significant uncertainty. To account for the uncertainty arising from the randomness of the observed independent individuals and their limited sample size, we employ the bootstrap augmenting the sample size to  $n_{\text{boot}} > n$  individuals. To generate spatially correlated tracks so as to reflect the gregarious behavior typical of herds, we sample the random moves for each resampled individual. This bootstrapped data augmentation procedure is repeated multiple times, and the pointwise  $(1 - \alpha)$  quantiles of the resulting bootstrapped

FIG 2. Test functions for propensity map  $\mu_0$ 

propensity estimates provide a measure of uncertainty. However, the universal threshold  $\lambda_\alpha^{\text{QUT}}$  used to select the regularization parameter  $\lambda$  tends to be conservative, shrinking the total variation differences of the propensity estimates toward zero and introducing bias. To improve both the estimation accuracy and the coverage properties of the uncertainty intervals, we apply a pointwise bias correction  $\hat{\mu}^{\text{bc}} = 2\hat{\mu} - \bar{\mu}^{\text{boot}}$ , where  $\bar{\mu}^{\text{boot}}$  represents the averaged bootstrapped propensity estimates (Efron & Tibshirani 1993). We apply the data augmentation and uncertainty quantification in to the Cervid dataset using  $n_{\text{boot}} = 600$  and 1000 sampled locations for each bootstrap individual with 100 runs.

### 3. Monte Carlo simulation

#### 3.1. Estimation of disease propensity maps

We generate an entire population of  $n_0 = 5000$  individuals moving over a square fenced area  $\Omega_0$  made of  $N_0 \times N_0$  lattice with known propensity  $\mu_0$  given by one of the three binary profiles in Figure 2 which simulates (from left to right) a lake, a river or a lake plus a corner. We choose a full discretization with  $N_0 = 50$  to provide a fine mapping of the area. For individual  $i \in \{1, \dots, n_0\}$ , we simulate  $T = 2880$  random moves  $l_1^{(i)}, l_2^{(i)}, \dots, l_T^{(i)}$  on the lattice  $\Omega$ . The value of  $T = 2880$  mimics GPS samplings every  $t = 15$  minutes for 30 days. At each time, the proposed moves are either to stay at the current location or to move to one of its four neighbors. We simulate two different herd behaviors: one half of the individuals moves randomly with equal probability  $1/5$  to one of the five proposed moves, while the other half moves with a probability that depends on  $\mu_0$  in a way that doubles the probability of moving to a region of higher virus infection propensity. We call  $L_0$  the  $n_0 \times T$  matrix which entry  $(i, j)$  corresponds to the lattice locations of the  $i$ -th individual at time  $t$ . Based on  $L_0$ , we build the  $n_0 \times p_0$  matrix  $X_0$  which counts the time spent in each of the  $p_0 = N_0^2$  lattice locations of  $\Omega$  for each of the  $n_0$  individuals. Then we generate the binary infection vector  $\mathbf{y}_0$  whether the animal was infected during

the time period, according to model (1). We expect more ones in the entries of  $\mathbf{y}_0$  corresponding to the second herd which tends to stay in a region of higher virus infection propensity.

To investigate the impact of the spatial discretization of  $\Omega_0$ , we discretize it into  $(N \times N)$  lattices with  $N \in \{30, 50\}$ , the largest  $N$  corresponding to the full  $\Omega_0$  plotted in Figure 2. To investigate the impact of different frequencies of the tracers placed on the individuals, we sample the  $L_0$  matrix every  $t \in \{1, 96\}$  units, a unit being 15 minutes, which means that each tracer sends its current location either every 15 minutes or 24 hours. The corresponding matrix  $L_t$  of GPS locations built from taking every  $t$  columns of  $L_0$  has 2880, or 720 columns, leading to a regression matrix  $X$  of size  $n_0 \times p$ , where  $p = N^2$ . Finally the number of tracers placed on the full population, that is, the number of observations, is taken as  $n \in \{500, 5000\}$ , the largest  $n$  corresponding to the full population  $n_0 = 5000$ .

For increasing sample sizes  $n \in \{500, 5000\}$ , increasing spatial discretization  $N \in \{30, 50\}$ , increasing temporal frequencies  $1/t$  with  $t \in \{96, 1\}$ , we perform Monte Carlo simulations for each combination of the three propensity maps  $\boldsymbol{\mu}_0$  plotted in Figure 2. Each scenario is simulated 100 times, leading to 100 full data information triplets  $(\mathbf{y}_0, L_0, X_0)$ , from which a response vector  $\mathbf{y}$  is extracted and a regression matrix  $X$  is built, depending on the value of  $(n, N, t)$ . For each of the 100 data sets generated, we estimate the propensity map with our total variation estimator solution to (2) with the quantile universal threshold of Definition 2.2 for the value of  $\lambda$ . For comparison we also estimate the propensities using three approaches: splines using `mgcv` R package (Wood 2001), a naive empirical estimate

$$\hat{\mu}_m^{\text{emp}}(\omega^{j,k}) = \frac{\sum_{\{i|y_i=1\}} x_i^{j,k}}{\sum_{i=1}^n x_i^{j,k}} \quad (5)$$

and its smoothed version using Gaussian process regression (GPR) on the log-odds

$$\log \left( \frac{\hat{\mu}_m^{\text{emp}}(\omega^{j,k})}{1 - \hat{\mu}_m^{\text{emp}}(\omega^{j,k})} \right). \quad (6)$$

Regularization parameters for splines and GPR were chosen with cross-validation. Owing to the different values of  $(n, N, t)$ , we scale both the total variation, the splines, the empirical, and the GPR estimates on the interval  $[0, 1]$  to compare them in terms of mean squared error calculated as  $\text{MSE} = \sum_{l=1}^p (\hat{\mu}_l - \tilde{\mu}_{0,l})^2 / p$ , where  $\tilde{\mu}_0$  is the nearest-neighbor interpolation of  $\boldsymbol{\mu}_0$  on a coarser scale and  $p = N^2$ .

Table 1 reports the MSE between  $\hat{\boldsymbol{\mu}}$  and  $\tilde{\boldsymbol{\mu}}_0$  averaged over the 100 Monte Carlo runs. Figure 3 shows typical estimations for the two propensity maps considered (`river` and `lake+corner`). Our method outperforms in nearly all scenarios. Splines tend to underestimate high propensity regions. As expected, MSE decreases for the asymptotic we considered, namely when the sample size  $n$  of individuals increases, the spatial discretization  $N$  increases, and the GPS frequency  $1/t$  increases.

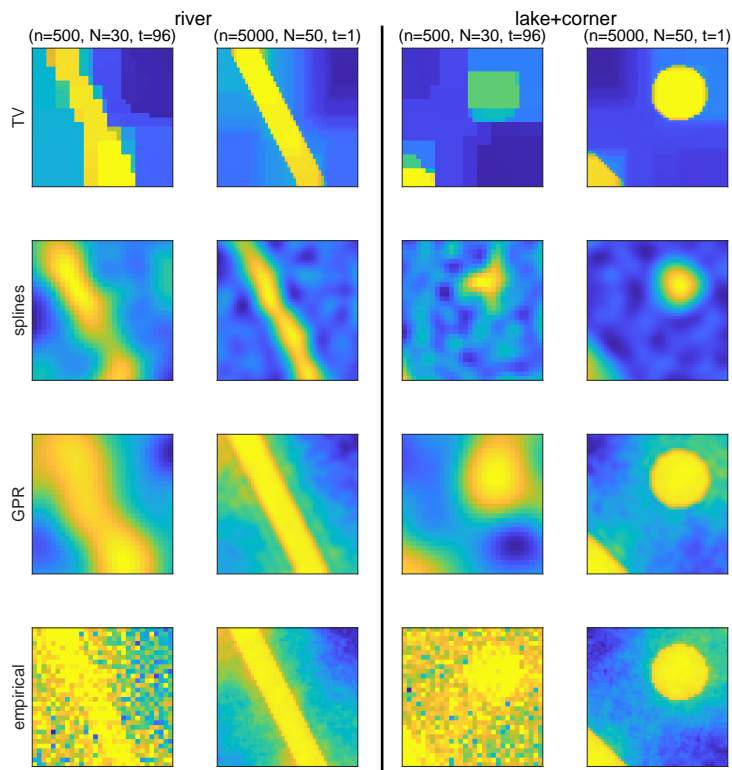


FIG 3. Increasing performance based on  $(n, N, t)$  from  $(500, 30, 96)$  to  $(5000, 50, 1)$  for all estimators, *river* and *lake+corner* propensity maps.

### 3.2. Coverage probability

We assess coverage probability of the bootstrap-based data augmentation and uncertainty quantification method outlined in Section 2.4 using the parameters  $(n, N, t) = (500, 30, 1)$ , with  $n_{\text{boot}} = 5000$  bootstrap individuals and 720 sampled locations for each bootstrap individual. A Monte Carlo simulation with 100 iterations, summarized in Table 2, evaluates the (MSE) of the bootstrap estimator, alongside the average coverage proportion and the average width of the point-wise confidence intervals. Targeting a nominal coverage level of 0.95, the total variation (TV) method exhibits reasonable coverage. Other methods show notably lower coverage. Compared with same  $(n, N, t)$  setting in Table 1, the bootstrap estimate considerably improves the MSE for all estimators and simulated maps. Overall, the TV method demonstrates good performance with better coverage while maintaining reasonably sized confidence intervals. This suggests that our method provides a useful framework for practitioners to assess the significance of key propensity regions. To illustrate the uncertainty measures, Figure 4 presents typical point-wise uncertainty intervals for the four

TABLE 1

Results of Monte Carlo simulation reporting the averaged mean squared errors between  $\hat{\mu}$  (TV, splines, GPR and empirical) and  $\mu_0$  (lake, river and lake + corner) over 100 runs for combinations of  $(n, N, t)$ . In bold the best estimator for every setup.

N	t	n = estimator	Estimated MSE					
			500		5000		500	
			lake		river		lake+corner	
30	96	TV	<b>0.165</b>	<b>0.123</b>	<b>0.367</b>	0.392	<b>0.228</b>	<b>0.217</b>
		splines	0.281	0.190	0.395	<b>0.256</b>	0.302	0.226
		GPR	0.421	0.360	0.541	0.471	0.439	0.385
		empirical	0.709	0.460	0.740	0.545	0.729	0.491
	1	TV	<b>0.163</b>	<b>0.120</b>	<b>0.363</b>	0.380	<b>0.226</b>	<b>0.208</b>
		splines	0.274	0.190	0.390	<b>0.255</b>	0.301	0.227
		GPR	0.440	0.345	0.528	0.459	0.455	0.370
		empirical	0.462	0.349	0.545	0.463	0.478	0.375
50	96	TV	<b>0.160</b>	<b>0.130</b>	0.398	<b>0.243</b>	<b>0.233</b>	<b>0.159</b>
		splines	0.281	0.191	<b>0.394</b>	0.259	0.301	0.231
		GPR	0.414	0.377	0.533	0.482	0.438	0.400
		empirical	0.750	0.530	0.774	0.597	0.765	0.548
	1	TV	<b>0.148</b>	<b>0.124</b>	0.393	<b>0.234</b>	<b>0.225</b>	<b>0.151</b>
		splines	0.277	0.191	<b>0.392</b>	0.260	0.303	0.232
		GPR	0.466	0.353	0.542	0.457	0.481	0.375
		empirical	0.488	0.359	0.561	0.462	0.507	0.381

estimators based on the lake simulated profile.

TABLE 2

Results of Monte Carlo simulation reporting the averaged mean squared errors between  $\hat{\mu}^{bc}$  and  $\mu_0$ , the averaged coverage probability (for a target value of 0.95) and the averaged width of the point-wise bootstrap confidence intervals over 100 runs, for four estimators  $\hat{\mu}$  (TV, splines, GPR and empirical); for the three propensity maps  $\mu_0$  (lake, river and lake + corner) for  $(n, N, t) = (500, 30, 1)$ ,  $n_{boot} = 5000$ , and 720 sampled locations for each bootstrap individual.

estimator	Average MSE, coverage and width								
	lake			river			lake+corner		
	MSE	coverage	width	MSE	coverage	width	MSE	coverage	width
TV	0.036	0.843	0.322	0.215	0.778	0.820	0.072	0.817	0.500
splines	0.124	0.288	0.426	0.146	0.265	0.418	0.124	0.225	0.353
GPR	0.201	0.313	0.324	0.278	0.331	0.358	0.215	0.384	0.356
empirical	0.222	0.274	0.346	0.297	0.276	0.366	0.233	0.358	0.384

#### 4. Application to white-tailed deer data

We now go back to the data described in Section 1.2 and we apply the discussed method. Figure 5 displays the estimated profiles obtained using our TV approach along with the associated point-wise confidence intervals (left panel). The right panel presents the observed abundance of *C. stellifer*, a known vector of EHDV. Figure 6 compares the EHDV-1 propensities estimated with four different methods.

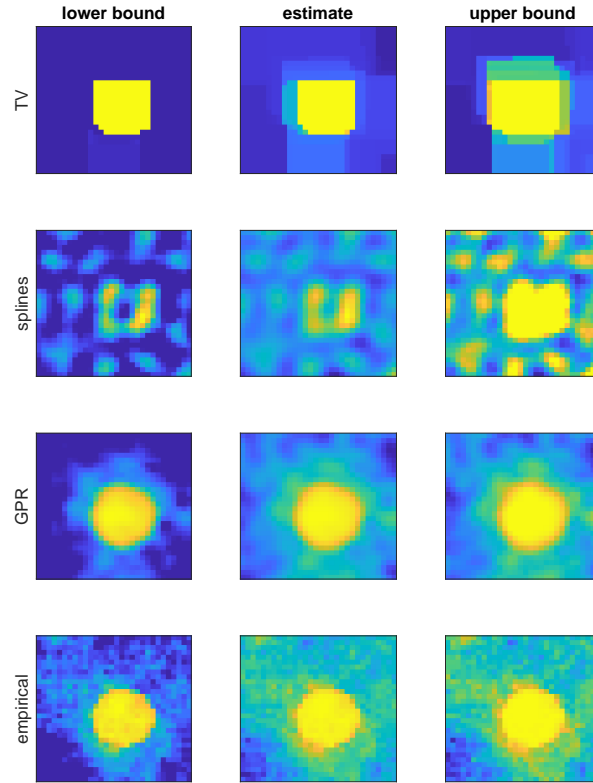


FIG 4. Estimated profiles and point-wise uncertainty quantification lower and upper bounds of estimated lake propensity maps for all estimators, for fixed  $(n, N, t) = (500, 30, 1)$ ,  $n_{boot} = 5000$  and 720 sampled locations for each bootstrapped individual.

Compared to the other models of disease risk estimation, TV points to smaller areas in which surveillance should be intensified for EHDV. It effectively pinpoints two specific feeders associated with EHDV-1 risk, despite having no prior knowledge of their locations. These two feeders have particularly high relative abundance of both Parous and Gravid *C. stellifer* which supports the risk estimation. In comparison, GPR and the empirical models suggest that the only area where disease risk is low is the northeastern region of the ranch. Such estimates make unlikely the surveillance or control efforts since that would require controlling the abundance of *C. stellifer* on 140 ha. Instead, the TV model suggests that the efforts should focus on the southeastern section and two supplementation feeders in the western portion. This reduces the initial control and surveillance area substantially. The splines model provided the most similar results to TV, albeit a larger risk area. Nonetheless, the splines model correlated well with the abundance of both Gravid and Parous *C. stellifer*.

In addition to outperforming other methods, our approach offers valuable in-

sights into the spatial distribution of disease risk across the ranch. For EHDV-1, the southwestern area was identified as having the highest disease risk (Figure 5), despite the relatively low abundance of *C. stellifer*. This unexpected finding suggests that midges in this region may have a higher relative prevalence of EHDV-1 compared to other areas, an insight that would not emerge from analyzing vector distribution alone. For EHDV-2, the method indicates that nearly the entire study area is at high risk, with the exception of a small region near a feeder in the north-central part of the ranch (Figure 5; Benn et al. (2024)). This pattern may reflect more extensive movement of animals infected with EHDV-2 or a higher prevalence of EHDV-2 during the study period. For EHDV-6, the eastern region of the ranch was highlighted as a high-risk area. This result aligns with the abundance of vectors in the region and underscores the importance of gravid *C. stellifer* (Dinh, Gomez, Orange, Morris, Sayler, McGregor, Blosser, Burkett-Cadena, Wisely & Blackburn 2021), which were more abundant than parous individuals in the northeastern part of the ranch. Interestingly, none of the models for EHDV-1 or EHDV-6 predicted high disease risk in the northeastern portion. These results can be interpreted in the context of the distribution and abundance of *Culicoides* vectors across the ranch, as determined through vector collection conducted in parallel with animal tracking studies.

## 5. Conclusion

We introduce an innovative model that extends tomographic methodologies to estimate landscape susceptibility to various risks using GPS data, in a manner analogous to Positron Emission Tomography (PET). By adapting tomographic principles to interpret spatial data from GPS signals, our model indirectly assesses landscape-related risks, broadening tomography’s application beyond medical imaging. Our approach uniquely predicts disease transmission risk without requiring detailed knowledge of vector ecology or environmental conditions, distinguishing it from traditional models that rely on extensive host movement and vector presence data. The sample size required and the time series length will depend on the geographical extent, ecology of the disease and movement ecology of the animals.

In addition to developing this novel approach, we propose a solution based on Total Variation with a selection of its smoothing parameter. We validate our approach with WTD data, observing alignment with known EHDV risks and vector ecology, while providing additional insights to investigate. Comparative analyses reveal our model’s performance exceeds that of conventional spatial statistical and inverse problem-solving approaches, underscoring its robustness and adaptability. While individual recapture data is required—posing challenges for certain species—the model is applicable in contexts where movement tracking is feasible, such as avian malaria research.

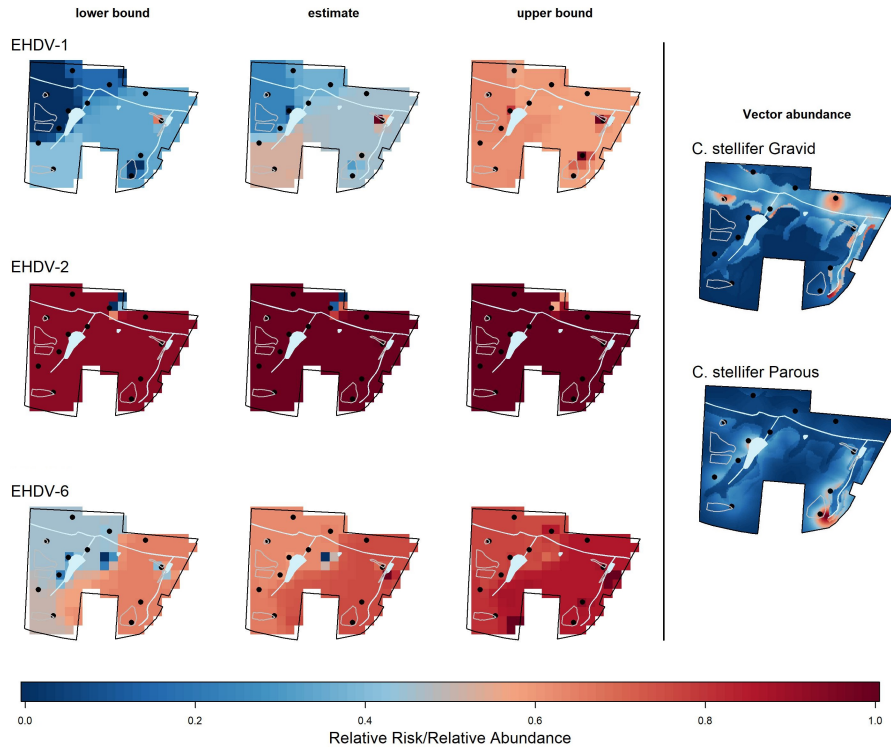


FIG 5. EHDV-1, EHDV-2 and EHD-6 disease risk estimation in white tailed deer and three exotic cervid species in a Florida ranch. The left column panels show the lower bound, estimate and upper bound of the relative disease risk for each of the three serotypes evaluate based on TV model. Warmer colors show higher risk of getting infected. The right panels show the average relative abundance of *Culicoides stellifer* in week 14 of 2015 and 2016. *C. stellifer* is a competent vector of EHDV.

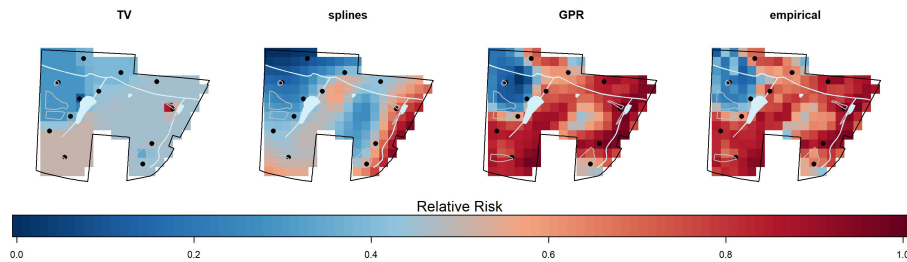


FIG 6. EHDV-1 disease risk estimation in white tailed deer and three exotic cervid species in a Florida ranch, using four different methods.

References

Ahmed, S., Mcinerny, G., O’Hara, K., Harper, R., Salido, L., Emmott, S. & Joppa, L. (2015), ‘Scientists and software - surveying the species distribution

- modeling community', *Diversity and Distributions* **21**.
- Albery, G., Sweeny, A., Becker, D. & Bansal, S. (2022), 'Fine-scale spatial patterns of wildlife disease are common and understudied', *Functional Ecology* **36**(1), 214–225.
- Benn, J. S., Orange, J. P., Gomez, J. P., Dinh, E. T., McGregor, B. L., Blosser, E. M., Burkett-Cadena, N. D., Wisely, S. M. & Blackburn, J. K. (2024), 'Culicoides midge abundance across years: Modeling inter-annual variation for an avian feeder and a candidate vector of hemorrhagic diseases in farmed wildlife', *Viruses* **16**(5), 766.
- Brdar, S., Gavrić, K., Čulibrk, D. & Crnojević, V. (2016), 'Unveiling spatial epidemiology of hiv with mobile phone data', *Scientific reports* **6**(1), 19342.
- Bühlmann, P. & van de Geer, S. (2011), *Statistics for High-Dimensional Data: Methods, Theory and Applications*, Springer, Heidelberg.
- Cauvin, A., Dinh, E., Orange, J., Shuman, R., Blackburn, J. & Wisely, S. (2020), 'Antibodies to epizootic hemorrhagic disease virus (ehdv) in farmed and wild florida white-tailed deer (*odocoileus virginianus*)', *Journal of wildlife diseases* **56**(1), 208–213.
- de Thoisy, B., Silva Oliveira, N., Sacchetto, L., de Souza Trindade, G. & Drumond, B. (2020), 'Spatial epidemiology of yellow fever: Identification of determinants of the 2016-2018 epidemics and at-risk areas in brazil', *PLoS neglected tropical diseases* **14**(10), e0008691.
- Dinh, E., Cauvin, A., Orange, J., Shuman, R., Wisely, S. & Blackburn, J. (2020), 'Living la vida t-locoh: Site fidelity of florida ranched and wild white-tailed deer (*odocoileus virginianus*) during the epizootic hemorrhagic disease virus (ehdv) transmission period', *Movement ecology* **8**, 1–9.
- Dinh, E., Gomez, J., Orange, J., Morris, M., Sayler, K., McGregor, B., Blosser, E., Burkett-Cadena, N., Wisely, S. & Blackburn, J. (2021), 'Modeling abundance of culicoides stellifer, a candidate orbivirus vector, indicates nonrandom hemorrhagic disease risk for white-tailed deer (*odocoileus virginianus*)', *Viruses* **13**(7), 1328.
- Dinh, E., Orange, J., Peters, R., Wisely, S. & Blackburn, J. (2021), 'Resource selection by wild and ranched white-tailed deer (*odocoileus virginianus*) during the epizootic hemorrhagic disease virus (ehdv) transmission season in florida', *Animals* **11**(1), 211.
- Donoho, D. L. (1995), 'Nonlinear solution of linear inverse problems by wavelet-vaguelette decomposition', *Applied and Computational Harmonic Analysis* **2**(2), 101–126.
- Dougherty, E., Seidel, D., Blackburn, J., Turner, W. & Getz, W. (2022), 'A framework for integrating inferred movement behavior into disease risk models', *Movement ecology* **10**(1), 1–15.
- Dougherty, E., Seidel, D., Carlson, C., Spiegel, O. & Getz, W. (2018), 'Going through the motions: incorporating movement analyses into disease research', *Ecology letters* **21**(4), 588–604.
- Efron, B. & Tibshirani, R. (1993), *An introduction to the bootstrap*, Chapman and Hall, London; New York.
- Elith, J., Phillips, S., Hastie, T., Dudik, M., Chee, Y. & Yates, C. (2011), 'A

- statistical explanation of maxent for ecologists', *Diversity and Distributions* **17**(1), 43–57.
- Frias-Martinez, V., Rubio, A. & Frias-Martinez, E. (2012), Measuring the impact of epidemic alerts on human mobility using cell-phone network data, in 'Second Workshop on Pervasive Urban Applications@ Pervasive', Vol. 12.
- Giacobino, C., Sardy, S., Diaz-Rodriguez, J. & Hengardner, N. (2017), 'Quantile universal threshold', *Electronic Journal of Statistics* **11**, 4701–4722.
- Harvell, C., Mitchell, C., Ward, J., Altizer, S., Dobson, A., Ostfeld, R. & Samuel, M. (2002), 'Climate warming and disease risks for terrestrial and marine biota', *Science (New York, N.Y.)* **296**, 2158–62.
- Hollingsworth, T., Pulliam, J., Funk, S., Truscott, J., Isham, V. & Lloyd, A. (2015), 'Seven challenges for modelling indirect transmission: Vector-borne diseases, macroparasites and neglected tropical diseases', *Epidemics* **10**.
- Killilea, M., Swei, A., Lane, R., Briggs, C. & Ostfeld, R. (2008), 'Spatial dynamics of lyme disease: A review', *EcoHealth* **5**, 167–95.
- Kirby, R., Delmelle, E. & Eberth, J. (2017), 'Advances in spatial epidemiology and geographic information systems', *Annals of Epidemiology* **27**.
- Lima, A., De Domenico, M., Pejovic, V. & Musolesi, M. (2015), 'Disease containment strategies based on mobility and information dissemination', *Scientific reports* **5**(1), 1–13.
- McGregor, B., Sloyer, K., Sayler, K., Goodfriend, O., Krauer Campos, J., Acevedo, C., Zhang, X., Mathias, D., Wisely, S. & Burkett-Cadena, N. (2019), 'Field data implicating *Culicoides stellifer* and *Culicoides venustus* (diptera: Ceratopogonidae) as vectors of epizootic hemorrhagic disease virus', *Parasites & vectors* **12**, 1–13.
- McGregor, B., Stenn, T., Sayler, K., Blosser, E., Blackburn, J., Wisely, S. & Burkett-Cadena, N. (2019), 'Host use patterns of *Culicoides* spp. biting midges at a big game preserve in florida, usa, and implications for the transmission of orbiviruses', *Medical and veterinary entomology* **33**(1), 110–120.
- Messina, J., Brady, O., Pigott, D., Golding, N., Kraemer, M., Scott, T., Wint, W., Smith, D. & Hay, S. (2015), 'The many projected futures of dengue', *Nature Reviews Microbiology* **13**, 230–239.
- Morris, L. & Blackburn, J. (2016), 'Predicting disease risk, identifying stakeholders, and informing control strategies: A case study of anthrax in montana', *EcoHealth* **13**(2), 262–273.
- Nelder, J. A. & Wedderburn, R. W. M. (1972), 'Generalized linear models', *Journal of the Royal Statistical Society: Series A* **135**(3), 370–384.
- Orange, J., Dinh, E., Goodfriend, O., Citino, S., Wisely, S. & Blackburn, J. (2021), 'Evidence of epizootic hemorrhagic disease virus and bluetongue virus exposure in nonnative ruminant species in northern florida', *Journal of Zoo and Wildlife Medicine* **51**(4), 745–751.
- Orange, J., Dinh, E., Peters, R., Wisely, S. & Blackburn, J. (2021), 'Inter-annual home range fidelity of wild and ranched white-tailed deer in florida: implications for epizootic hemorrhagic disease virus and bluetongue virus intervention', *European Journal of Wildlife Research* **67**, 1–8.
- Ostfeld, R., Glass, G. & Keesing, F. (2005), 'Spatial epidemiology: an emerging

- (or re-emerging) discipline', *Trends in Ecology and Evolution* **20**(6), 328 – 336.
- Patz, J. A., Olson, S. H., Uejio, C. K. & Gibbs, H. K. (2008), 'Disease emergence from global climate and land use change', *Medical Clinics of North America* **92**(6), 1473–1491.
- Ragg, J. & Moller, H. (2000), 'Microhabitat selection by feral ferrets (*Mustela furo*) in a pastoral habitat, east otago, new zealand', *New Zealand Journal of Ecology* pp. 39–46.
- Riley, S., Eames, K., Isham, V., Mollison, D. & Trapman, P. (2015), 'Five challenges for spatial epidemic models', *Epidemics* **10**, 68 – 71. Challenges in Modelling Infectious Disease Dynamics.
- Rudin, L. I., Osher, S. & Fatemi, E. (1992), 'Nonlinear total variation based noise removal algorithms', *Physica D* **60**, 259–268.
- Sardy, S., Diaz-Rodriguez, J. & Giacobino, C. (2022), 'Thresholding tests based on affine lasso to achieve non-asymptotic nominal level and high power under sparse and dense alternatives in high dimension', *Comput. Stat. Data Anal.* **173**(C).
- Sardy, S. & Monajemi, H. (2019), 'Efficient threshold selection for multivariate total variation denoising', *Journal of Computational and Graphical Statistics* **28**(1), 23–35.
- Stallknecht, D., Luttrell, M., Smith, K. & Nettles, V. (1996), 'Hemorrhagic disease in white-tailed deer in texas: a case for enzootic stability', *Journal of wildlife Diseases* **32**(4), 695–700.
- Stockwell, D. (1999), 'The garp modelling system: problems and solutions to automated spatial prediction', *International journal of geographical information science* **13**(2), 143–158.
- Tibshirani, R. (1996), 'Regression shrinkage and selection via the lasso', *Journal of the Royal Statistical Society, Series B* **58**(1), 267–288.
- Torres-Sorando, L. & Rodriguez, D. (1997), 'Models of spatio-temporal dynamics in malaria', *Ecological Modelling* **104**(2), 231 – 240.
- Wahba, G. (1990), *Spline Models for Observational Data*, Society for Industrial and Applied Mathematics, Philadelphia.
- Wood, S. N. (2001), 'mgcv: Gams and generalized ridge regression for r', *R news* **1**(2), 20–25.

## APPENDIX

### A. Proof of Property 2.1

The negative log-likelihood associated to model

$$\mathbf{Y} \sim \text{Bernoulli}(g^{-1}(X\boldsymbol{\mu}))$$

is

$$h(\boldsymbol{\mu}; \mathbf{y}) := -\log L(g^{-1}(X\boldsymbol{\mu}); \mathbf{y}) = \sum_{i=1}^n y_i \log(1 + \exp(-\mathbf{x}_i^T \boldsymbol{\mu})) + \sum_{i=1}^n (1 - y_i) \log(1 + \exp(\mathbf{x}_i^T \boldsymbol{\mu})).$$

Let  $D$  be the  $q \times p$  matrix of the  $q$  finite differences such that  $\|D\boldsymbol{\mu}\|_1 = \sum_{l=1}^p \sum_{l' \in \partial l} |\mu_l - \mu_{l'}|$ . Since all differences between neighbors are penalized and there are more finite differences than elements in the partition of  $\Omega$  (that is,  $q > p$ ), the kernel of  $D$  is spanned by the constant vector. Moreover the cost function

$$\min_{\boldsymbol{\mu} \in \mathbb{R}^p} -\log L(g^{-1}(X\boldsymbol{\mu}); \mathbf{y}) + \lambda \sum_{l=1}^p \sum_{l' \in \partial l} |\mu_l - \mu_{l'}|, \quad (7)$$

is continuous in  $\boldsymbol{\mu}$  and defined on  $\mathbb{R}^p$ , a closed set. The function  $h$  is bounded from below by zero and the penalty term tends to infinity unless  $\boldsymbol{\mu}$  is in the kernel of  $D$ . Since all entries of  $X$  are positive (they are total times) and each row of  $X$  has at least one strictly positive entry (an animal is part of the study if he spent some time in the ranch), the entries of  $X\mathbf{1}$  are strictly positive; consequently, it is easy to check that  $\lim_{\epsilon \rightarrow \pm\infty} h(\epsilon\mathbf{1}; \mathbf{y}) = +\infty$  under the assumption the entries of  $\mathbf{y}$  are not all ones or all zeros. So the cost function (7) is coercive. Weierstrass theorem guarantees a minimum in  $\mathbb{R}^p$  for any given  $\lambda > 0$ .

The cost function (7) is moreover convex, and the Lagrange function associated to it is

$$\mathcal{L}(\boldsymbol{\mu}, \boldsymbol{\gamma}, \boldsymbol{\omega}) = h(\boldsymbol{\mu}; \mathbf{y}) + \lambda \|\boldsymbol{\gamma}\|_1 + \boldsymbol{\omega}^T (D\boldsymbol{\mu} - \boldsymbol{\gamma}).$$

So the Lagrangian dual problem of (7) is

$$\max_{\|\boldsymbol{\omega}\|_\infty \leq \lambda} \min_{\boldsymbol{\mu}} h(\boldsymbol{\mu}; \mathbf{y}) + \boldsymbol{\mu}^T D^T \boldsymbol{\omega}.$$

Consequently there exists a finite  $\lambda$  that leads to the constant MLE estimate, given by

$$\min_{\boldsymbol{\omega} \in \mathbb{R}^q} \|\boldsymbol{\omega}\|_\infty \quad \text{s.t.} \quad \nabla_{\boldsymbol{\mu}} h(\boldsymbol{\mu}; \mathbf{y}) + D^T \boldsymbol{\omega} = \mathbf{0}, \quad \boldsymbol{\mu} = \hat{\beta}_0 \mathbf{1}, \quad \hat{\beta}_0 = \underset{\beta_0}{\operatorname{argmin}} h(\beta_0 \mathbf{1}; \mathbf{y}).$$

### B. Power of the TV-test

We evaluate with a Monte Carlo simulation the power of the TV-test of Section 2.3 as a function of the sample size  $n$  under the fixed alternative hypothesis

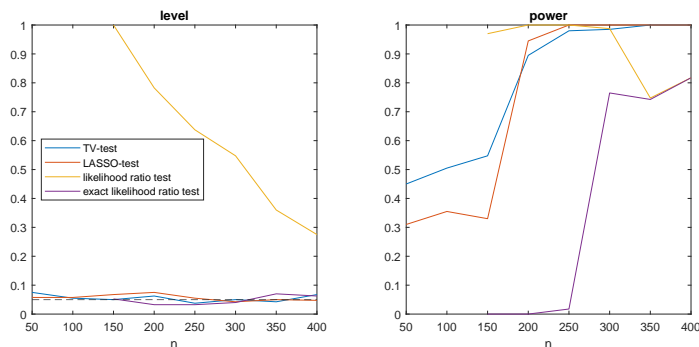


FIG 7. Plots of the level (left) and of the power (right) of four tests as a function of sample size  $n$ : TV-test, LASSO-test, the likelihood ratio test based either on the asymptotic  $\chi^2$  distribution or on the exact distribution empirically sampled.

that the propensity is the **lake+corner** map. Figure 7 reports the level (left plot) and the power (right plot) of four tests: the TV-test (4) and the LASSO-test (Sardy et al. 2022), the likelihood ratio test based on the asymptotic  $\chi^2$  distribution, and the exact likelihood ratio test.

As far as level is concerned (here  $\alpha = 0.05$ ), one observes that the likelihood ratio test using the asymptotic  $\chi^2$  distribution is far from its nominal level when  $n$  is small. Not based on asymptotic, the other three tests achieve near nominal level (thanks to a Monte Carlo simulation to evaluate empirically the distribution of their respective test statistics under the null).

As far as power is concerned, the right plot of Figure 7 reveals that under an alternative hypothesis with spatial coherence like the **lake+corner** map, the TV-test is more powerful than the exact likelihood ratio test and the LASSO-test. The latter would be more powerful under a sparse alternative hypothesis since the LASSO penalty helps detect sparsity and the TV penalty helps detect spatial coherence.

### C. Data summary table

Table 3 summarizes raw data and shows the animal tracks that were used to estimate the disease risk of three EHDV serotypes in White-tailed deer and three exotic Cervid species. We show Animal ID, sex, tracking year, start and end date of tracking period, total number of days each animal was tracked and whether the animal was seronegative (0) or seropositive (1) for each serotype at the end of the tracking period. NA values indicate animals for which serostatus was unavailable. All animals were seronegative at the beginning of the tracking period. OV indicates *Odocoileus virginianus*, White-tailed deer. DD indicates *Dama dama*, Fallow deer. ED indicates *Elaphurus davidianus*, Pere David deer. CC indicates *Cervus canadensis*, Elk deer.

TABLE 3  
 Table summarizing raw data from White-tailed deer and three exotic Cervid species tracked to estimate the disease risk of three EHDV serotypes

Accession ID	Sex	Year	Date Collared	Date End	Days	EHDV-1	EHDV-2	EHDV-6
2015_OV10	M	2015	5/27/15	11/3/15	160	1	1	0
2015_OV11	F	2015	5/29/15	10/13/15	137	0	NA	0
2015_OV12	M	2015	5/27/15	9/23/15	119	1	1	0
2015_OV6	M	2015	5/28/15	10/3/15	128	1	NA	0
2015_OV7	M	2015	5/29/15	10/13/15	137	1	1	0
2015_OV8	M	2015	5/28/15	10/13/15	137	1	NA	0
2015_OV9	M	2015	5/27/15	10/3/15	129	1	0	0
OV059	F	2016	4/13/16	9/21/16	161	1	1	1
OV062	M	2016	4/13/16	9/21/16	161	NA	1	1
OV063	F	2015	5/28/15	10/15/15	140	1	NA	0
OV063	F	2016	4/13/16	10/3/16	173	1	1	1
OV064	F	2016	4/14/16	9/17/16	156	1	1	1
OV065	M	2015	5/29/15	10/12/15	136	1	1	0
OV065	M	2016	4/14/16	9/21/16	160	1	1	1
OV067	M	2016	4/14/16	9/2/16	141	NA	NA	1
OV069	F	2016	4/14/16	10/4/16	173	1	1	NA
OV070	F	2016	4/14/16	9/22/16	161	1	1	1
OV071	M	2015	5/27/15	10/13/15	139	1	NA	1
OV071	M	2016	4/14/16	9/22/16	160	1	1	1
OV072	M	2016	4/14/16	9/21/16	160	NA	NA	0
OV073	M	2016	4/15/16	9/23/16	161	1	NA	1
OV074	M	2015	5/28/15	10/14/15	139	1	1	0
OV074	M	2016	4/15/16	9/21/16	159	1	1	1
DD001	F	2016	4/15/16	4/3/17	353	0	1	0
DD2015_1	M	2015	5/28/15	10/12/15	137	1	1	0
DD2015_2	M	2015	5/29/15	10/14/15	138	0	0	0
ED001	F	2016	4/15/16	9/21/16	159	1	1	0
ED2015_1	M	2015	5/29/15	10/12/15	136	0	1	0
CC2015_1	M	2015	5/27/15	9/2/15	98	1	1	1
CC2015_2	M	2015	5/29/15	10/12/15	136	0	1	0